

Effect of density value and gradient distribution on the deformation mechanism of foamed concrete

Xu, Liangliang; Li, Xi; Atif, Muhammad; Li, Yulong

DOI

[10.1016/j.tws.2023.111487](https://doi.org/10.1016/j.tws.2023.111487)

Publication date

2023

Document Version

Final published version

Published in

Thin-Walled Structures

Citation (APA)

Xu, L., Li, X., Atif, M., & Li, Y. (2023). Effect of density value and gradient distribution on the deformation mechanism of foamed concrete. *Thin-Walled Structures*, 196, Article 111487. <https://doi.org/10.1016/j.tws.2023.111487>

Important note

To cite this publication, please use the final published version (if applicable). Please check the document version above.

Copyright

Other than for strictly personal use, it is not permitted to download, forward or distribute the text or part of it, without the consent of the author(s) and/or copyright holder(s), unless the work is under an open content license such as Creative Commons.

Takedown policy

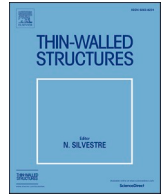
Please contact us and provide details if you believe this document breaches copyrights. We will remove access to the work immediately and investigate your claim.

Green Open Access added to TU Delft Institutional Repository

'You share, we take care!' - Taverne project

<https://www.openaccess.nl/en/you-share-we-take-care>

Otherwise as indicated in the copyright section: the publisher is the copyright holder of this work and the author uses the Dutch legislation to make this work public.



Full length article

Effect of density value and gradient distribution on the deformation mechanism of foamed concrete

Liangliang Xu^{a,b}, Xi Li^c, Muhammad Atif^{a,b}, Yulong Li^{a,b,*}^a School of Aeronautics, Northwestern Polytechnical University, Xi'an 710072, China^b Joint International Research Laboratory of Impact Dynamics and its Engineering Applications, Northwestern Polytechnical University, Xi'an 710072, China^c Faculty of Civil Engineering and Geoscience, Delft University of Technology, Stevinweg 1, 2628 CN, the Netherlands

ARTICLE INFO

Keywords:

Foamed concrete
Density
Gradient
Compressive behavior
Deformation mechanism

ABSTRACT

Foamed concrete is an essential material in engineering that can be categorized into two types based on density distribution, namely uniform foamed concrete (UFC) and gradient foamed concrete (GFC). However, there exists a research gap concerning the mesoscopic deformation mechanism of UFC and GFC. The objective of this research is to bridge this gap by examining the quasi-static compression characteristics of UFCs with three distinct densities and GFCs with different density sequences. The results reveal that the strength of pore walls significantly influences the failure mechanism of UFCs with varying densities. Specifically, UFCs with low density exhibit weak pore-wall strength, leading to stress concentration at the pore-wall junction. During compression, these weak pore walls are widely dispersed within the specimen, resulting in a powdering failure mode. Conversely, UFCs with high density possess stronger pore walls, which prevent the powdering failure mode by maintaining adequate pore-wall strength. Nevertheless, the existence of a dominant crack within the specimen results in a splitting failure mode. In the context of GFCs, deformation occurs in a sequence from low to high density, with each layer exhibiting a failure mode corresponding to its density. Note that the last-deforming layer in this brittle gradient foam cannot attain the strength of the corresponding uniform foam. This is due to the failure of the second layer, which results in uneven contact surfaces and prompts the third layer to crack simultaneously. Finally, a statistical model is developed to forecast the compressive Stress-strain curve of foamed concrete, demonstrating remarkable agreement with experimental data.

1. Introduction

Foamed concrete (FC) [1–4], a hybrid material that combines the characteristics of foam [5–7] and concrete [8–10], has proven to be a versatile asset in various engineering applications. It is distinguished by its superior energy absorption capabilities, high specific strength, and high specific stiffness [11,12]. Additionally, it provides robust structural support and can be produced on a large scale [13–15]. Hence, FC finds extensive application in aviation safety, infrastructure development, and transportation, including aircraft arresting systems [16,17], track subgrade fillers [18,19], and backfilling of underground engineering structures [20]. The complex internal pore structure and varying components of FC contribute to the influence on its compressive behavior. Density [21,22], pore characteristics [23,24], foaming agent [25], and inclusions [26–29] are among these parameters. For instance, the impact of density and the height-to-diameter ratio on the failure

characteristics of FC was investigated by Tan et al. [21]. It was observed that density has a greater influence on determining the failure modes of FC compared to the height-to-diameter ratio. Furthermore, external loading conditions such as temperature [30,31], strain rate [32,33], and multi-axial loading [34,35] also have an impact on the bearing capacity of FC. Experiments were carried out on FC with varying densities using a split Hopkinson pressure bar by Feng et al. [33]. They reported a notable strain-rate enhancement and density dependence of FC. It is important to mention that the porosity of FC significantly affects its compressive strength.

Porosity (p) refers to the proportion of pore volume to the overall material volume, which is linked to the relative density ($\bar{\rho}$) of the material. In particular, $p = 1 - \bar{\rho}$. Relative density refers to the proportion of the foam material's density compared to the density of its matrix material. From this definition, it can be inferred that greater porosity in FC results in lower relative density and consequently lower load-bearing

* Corresponding author.

E-mail address: liyulong@nwpu.edu.cn (Y. Li).<https://doi.org/10.1016/j.tws.2023.111487>

Received 11 September 2023; Received in revised form 28 November 2023; Accepted 12 December 2023

Available online 14 December 2023

0263-8231/© 2023 Elsevier Ltd. All rights reserved.

capacity. Therefore, many strength prediction models for FC are based on its porosity or relative density [36–41]. For example, Nambiar et al. [40] investigated the impact of composition on FC strength and discovered that the strength–porosity model is highly accurate and easy to use. Guo et al. [41] developed a calculation model that accounts for nonlinear mechanical behavior, including the influences of damage, density, and temperature, and obtained good prediction results. However, the current research mainly focuses on quantifying macroscopic compressive strength. The X-Ray Computed Tomography (X-CT) method [42–46] has contributed to recent advancements in analyzing the mesoscopic deformation mechanism of FC. However, further development is still necessary to facilitate the analysis of FC at the mesoscale.

Recent advancements in the study of gradient foam materials have been noteworthy. While achieving a completely uniform distribution of pores within foamed concrete is not feasible, it is possible to engineer the process such that the pores exhibit a distinct gradient trend along a specific direction. This type of material is referred to as Gradient Foamed Concrete (GFC). In GFC, where pores are distributed in a gradient manner, the compressive behavior significantly deviates from that of Uniform Foamed Concrete (UFC). It should be noted that the term UFC is used here for comparative purposes, acknowledging that pore distribution is inherently non-uniform. Research has shown that gradient foam tends to deform initially from the lowest density, progressively expanding layer by layer towards higher density regions, excluding the inertial effect due to high velocity impacts [47,48]. However, when the inertia effect, induced by higher impact velocity, becomes significant, the deformation extension of the gradient foam is determined by the interplay of density gradient distribution and impact velocity [49,50]. These deformation laws for gradient foams are not only applicable to plastic foams such as metallic foams [51] and polymer foams [52], but also extend to brittle foams like foamed concrete [53]. In contrast to the stress plateau observed in uniform foams, gradient foams display a step-hardening behavior. The sequential collapse of different density layers within the specimen is responsible for this phenomenon. The Stress–strain response of the gradient foam can be adjusted by manipulating the layering gradient and varying the thickness of each layer. Consequently, the pore distribution of gradient foam can be engineered to satisfy specific engineering requirements [51–56]. Recently, the compressive response of FC was analyzed by Xu et al. [57] using mesoscale finite element analysis to examine the effects of porosity, gradient, and impact velocity. According to their report, GFC induces initial deformation in the area with the greatest porosity (which corresponds to the lowest relative density) without considering the inertia effect. Novel attempts were made by Zhou et al. [53] to enhance the energy absorption capacity by stacking four FC specimens with varying densities (400, 600, 800, and 1000 kg/m³) in a GFC configuration. It was observed that the density difference between adjacent layers could mitigate the propagation of cracks and improve the mechanical performance of GFC. Nevertheless, there is a lack of research on GFC, especially in the experimental investigation of the deformation mechanism.

This paper aims to investigate how density affects the deformation mechanism of FC, considering both uniform and gradient densities. To achieve this, three types of FC with different densities are prepared, and GFC with various gradient distributions is designed by arranging stacking sequences. Quasi-static compression experiments are performed on both UFC and GFC to investigate the impact of density distribution on compressive strength and failure mode. The stress distribution in the specimen is analyzed using mesoscale finite element simulation to reveal the deformation process and failure mechanisms observed in experiments. Finally, a statistical model is presented to describe the compressive strength of foamed concrete, providing accurate predictions that are consistent with experimental results.

2. Experimental results and discussion

2.1. Specimen preparation

The experimental specimen was made from a combination of fast hard sulphoaluminate cement, fly ash, water, admixture CH₃COONa, foaming agent H₂O₂, and polypropylene fiber. To prepare the specimen, the cement slurry was first created by mixing cement, fly ash, and water as the gel material. Foaming agent was then added to create closed pores within the slurry. The resulting mixture was poured into cylindrical molds and left to harden. Following the process of solidification, the FC underwent division into cylindrical specimens measuring 80 mm in diameter and 30 mm in height. All specimens were then conditioned for 30 days. In this work, FC specimens were prepared with densities of around 150 kg/m³, 300 kg/m³ and 450 kg/m³ to distinguish them from the previous study where specimen densities ranged from 400 to 1000 kg/m³ [53]. UFC-L, UFC-M, and UFC-H refer to the uniform foamed concrete with lower density (~150 kg/m³), medium density (~300 kg/m³), and higher density (~450 kg/m³), correspondingly. The density of the matrix material corresponding to FC was measured to be approximately 1000 kg/m³ by grinding FC into a dense powder. Hence, the relative densities of the three specimens are approximately 0.15, 0.30, and 0.45, respectively. Moreover, the GFC is composed of three layers of UFC, each maintaining a consistent thickness with the UFC. The GFC-LMH represents a three-layer gradient foamed concrete with lower, medium, and higher density distributed along the loading direction. In this study, a control specimen consisting solely of stacked UFC-M is established to consider the effect of the stacked interfaces. The UFC-MMM is a three-layer uniform foamed concrete, with each layer maintaining a medium density (~300 kg/m³).

2.2. Experimental set-up

The FC specimens underwent quasi-static compression tests using a universal testing machine, following the ASTM D1621-16 standard. The specimens were placed between two parallel plates. To reduce surface friction, the contact surface between the specimen and steel plate was lubricated. The universal testing machine was utilized to ensure a consistent strain rate (0.001 s⁻¹) during the quasi-static loading. To capture the deformation process of the FC specimens, a digital camera (MER-1070-14U3C-L, Daheng Technology Ltd.) was placed in front of the testing machine. The resolution and sampling frequency were set to 1280 × 800 pixels and 14 fps, respectively. The compressive stress σ of the specimens was determined by dividing the load value F from the universal testing machine by the initial cross-sectional area A_0 of the specimen. The strain ε of specimens was determined by dividing the axial deformation length ΔL of the specimen by its initial axial length L_0 . The data processing involved deducting the rigid body displacement of the universal testing machine.

Fig. 1 illustrates three repeatability experiments performed on specimens UFC-H and GFC-LMH, that are chosen as representatives. However, because of the intricate nature of foamed concrete, there is a certain amount of variation in the peak stress. Overall, the results from the three tests conducted on both categories of specimens demonstrate satisfactory concurrence. Therefore, only one curve for each type of specimens is analyzed in the following. For specimen UFC-H (Fig. 1a), it exhibits typical mechanical characteristics of a foam material. Materials of this nature can be classified into three stages on the Stress–strain curve, specifically the elastic, plateau, and densification stages. In the elastic stage, the stress typically rises in a nearly linear manner as the deformation increases. During the plateau stage, the stress remains relatively consistent across a wide range of deformation. Afterward, the stress increases rapidly, indicating the onset of the densification stage. For specimen GFC-LMH (Fig. 1b), in contrast to UFC-H, the Stress–strain curve exhibits three distinct parts with varying stresses. The main reason is the existence of three layers of UFCs with varying densities.

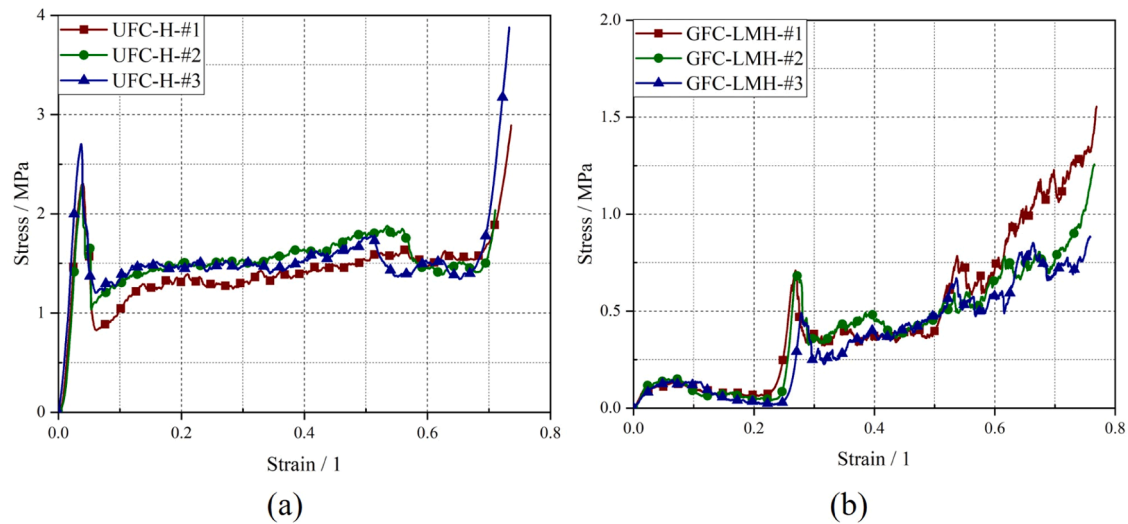


Fig. 1. Verification of experimental reproducibility: (a) UFC-H and (b) GFC-LMH.

2.3. Results of uniform density

Fig. 2 illustrates Stress–strain curves for varying densities of UFCs. The compression strength of higher-density UFC (UFC-H) is notably greater than that of lower-density specimens (UFC-M and UFC-L). Moreover, the UFC with greater density demonstrates a more noticeable strain-hardening characteristic, as the stress progressively rises with strain. This is due to the lower percentage of pores in higher-density specimens and more severe mutual contact of pore wall materials compared to low-density specimens. Consequently, with an increase in strain, a greater amount of material is engaged in the load-bearing procedure, resulting in the manifestation of strain-hardening characteristics.

Figs. 3 and 4 illustrate the deformation processes of UFC-L and UFC-H, respectively, revealing distinct failure modes and crack propagation processes for specimens with different densities. In UFC-L (Fig. 3), the collapse process started with the rupture of pore walls, followed by gradual crushing of failed pores until they turned into powder. No dominant cracks were observed during compression. On the other hand, UFC-H (Fig. 4) exhibited vertical cracks during compression, gradually propagating throughout the entire specimen, causing it to split into

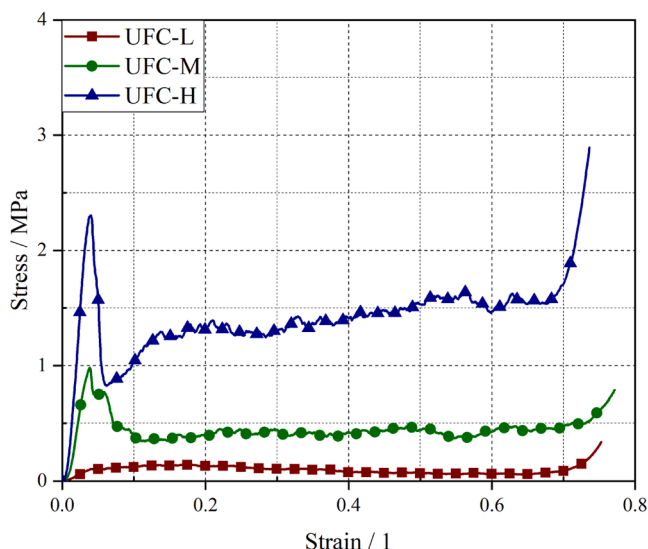


Fig. 2. Stress–strain curves of UFCs with different densities.

several pieces by individual cracks. The same failure mode has been noted in previous studies on foamed concrete with higher density (400–1000 kg/m³) [53]. The damage mode of UFC-M was intermediate between the powdering and splitting failure modes and is not presented here for simplicity.

The morphology of the specimen is shown in Fig. 5 following the completion of testing. At this point, the nominal strain is 0.8, indicating the complete collapse of the specimen. Fig. 5 indicates that the low-density UFC-L was severely powdering at the end of the compression process, while the higher-density UFCs left more noticeable broken pieces. The failure modes of UFCs with varying densities can be explicated as follows. The low-density specimen, characterized by a high number of pores and thin inter-pore walls, exhibits a lower load-bearing strength. Consequently, upon the initiation of damage, the pore walls fracture, culminating in a powdering failure mode. Conversely, specimens with higher densities, which possess fewer pores and thicker walls between them, demonstrate a higher load-bearing strength and fewer instances of pore wall breakage during failure. This results in the observation of large penetrating cracks, indicative of a splitting failure mode. Since the stress field distribution inside the specimens cannot be characterized experimentally, a finite element simulation in Section 4 will further discuss and demonstrate these observations.

2.4. Results of gradient density

The Stress–strain curves for UFC-MMM and GFC-LMH specimens are compared in Fig. 6. Despite having identical overall densities, these specimens exhibit different forms of density distribution, thus warranting their comparison. The second plateau stress stage of GFC-LMH mirrors that of UFC-MMM, given that the second layer of GFC-LMH possesses the same density as UFC-MMM. In contrast to UFC-MMM, GFC-LMH shows an early rise in stress after the second plateau. Uneven contact surfaces during the compression of the second layer have resulted in the emergence of cracks in the third layer of GFC-LMH. Consequently, the third layer of GFC-LMH can be perceived as containing an initial crack defect, a characteristic not observed in UFC-MMM. The aforementioned discussion is supported by the deformation process observed in the experiment, which is further elaborated on in the following section.

Figs. 7 and 8 display the deformation process of UFC-MMM and GFC-LMH, respectively, at different strains. In Fig. 7, despite being a three-layer stack, UFC-MMM shows no significant difference in failure modes among the layers, exhibiting both powdering and splitting failure modes. In contrast, GFC-LMH is structured with three separate layers of

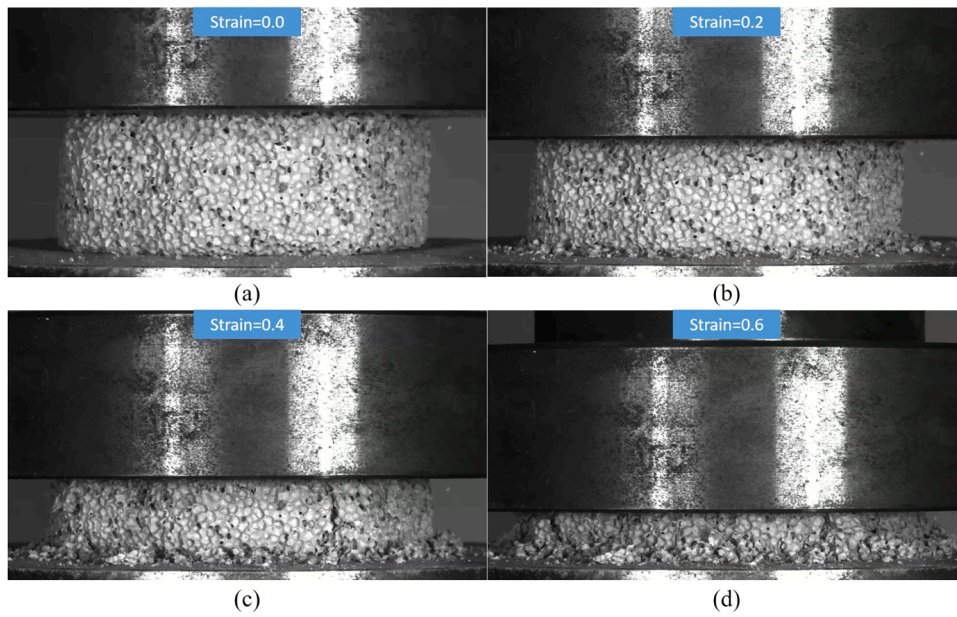


Fig. 3. Deformation process of uniform foamed concrete with low density ($\sim 150 \text{ kg/m}^3$) at different strains: (a) 0.0, (b) 0.2, (c) 0.4, and (d) 0.6.

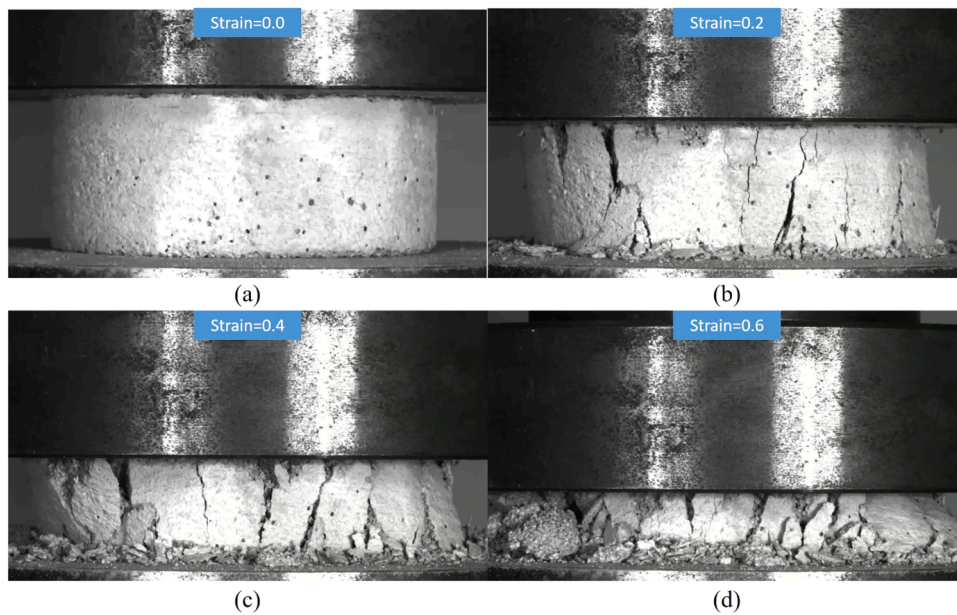


Fig. 4. Deformation process of uniform foamed concrete with higher density ($\sim 450 \text{ kg/m}^3$) at different strains: (a) 0.0, (b) 0.2, (c) 0.4, and (d) 0.6.

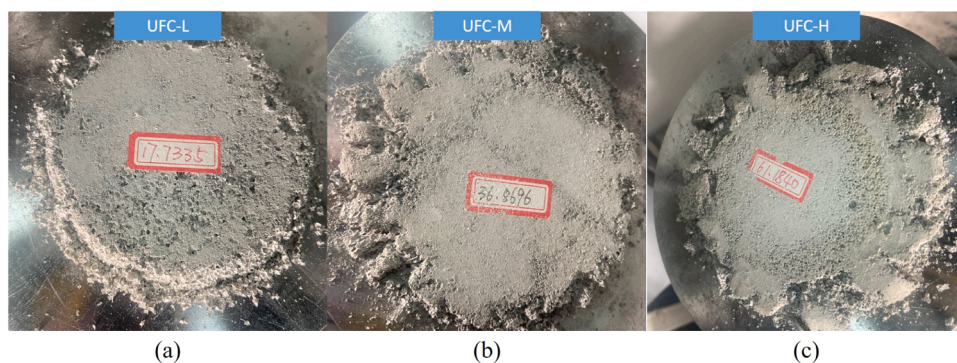


Fig. 5. Specimen morphology after experiments: (a) UFC-L, (b) UFC-M, and (c) UFC-H.

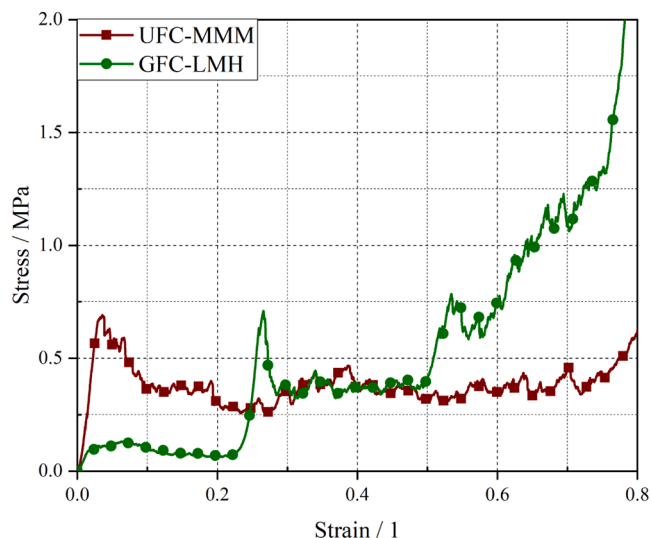


Fig. 6. Stress–strain curves of UFC-MMM and GFC-LMH for comparison.

UFCs, each displaying a varying density, as depicted in Fig. 8. The failure progression of GFC-LMH can be conceptualized as a sequential failure of the UFCs across the different layers, proceeding from the layer with the smallest density to that with the largest. This implies that the failure modes are predominantly dictated by the density of the respective layer. The UFC-L layer demonstrates a powdering failure mode, the UFC-H layer exhibits a splitting failure mode, while the UFC-M layer presents a failure mode that is intermediate between the two. Moreover, as depicted in Fig. 8c, in the event of the second layer's failure, cracks emerge in the third layer. It results in the absence of a plateau characteristic in the Stress–strain curve's third stage for GFC-LMH. This means that the interface is uneven due to the collapse of the second layer,

which in turn prevents the third layer from reaching its expected strength.

The Stress–strain curves for GFCs with different gradient configurations are compared in Fig. 9. Overall, GFC with various gradient configurations exhibit a similar trend and their values are closely matched. This suggests that under quasi-static loading conditions, the specimen reaches stress equilibrium at both ends and that GFC fails in order of increasing density. The deformation process of GFC-LHM is illustrated in Fig. 10. Irrespective of the stacking sequences of UFCs with varying densities, GFC always deforms in the order of density from low to high. Each layer exhibits failure modes corresponding to its respective density. The tests conducted in this study are limited to the quasi-static loading with a constant strain rate of 0.001 s^{-1} . Nevertheless, it is important to acknowledge that in cases of high-loading rates, the stress equilibrium between both ends of the specimen may be disrupted due to the inertial effect. At this point the gradient effect and the inertia effect jointly determine the mechanical response of GFCs. The conclusions of Fig. 9 cannot be generalized to this case.

3. Numerical results and discussion

The objective of the finite element simulations conducted with Abaqus/Explicit was to acquire the stress distribution within the specimen and elucidate the differences in failure modes of FC with varying porosities. Foam models at the mesoscale were generated utilizing the Voronoi diagram and the space holder technique [58]. First, a collection of spheres was produced based on the Voronoi diagram. Then, a solid model was formed by subtracting the combined volume of all spheres using Boolean operations, as depicted in Figs. 11a and 12b. The size of the sphere was set to 1.35 mm in diameter, while the model's geometry was adjusted to have a diameter and length of 10 mm each. This was done to strike a balance between computational accuracy and efficiency. To guarantee that the model accurately represents the research emphasis of the present study, the porosity in the model is kept

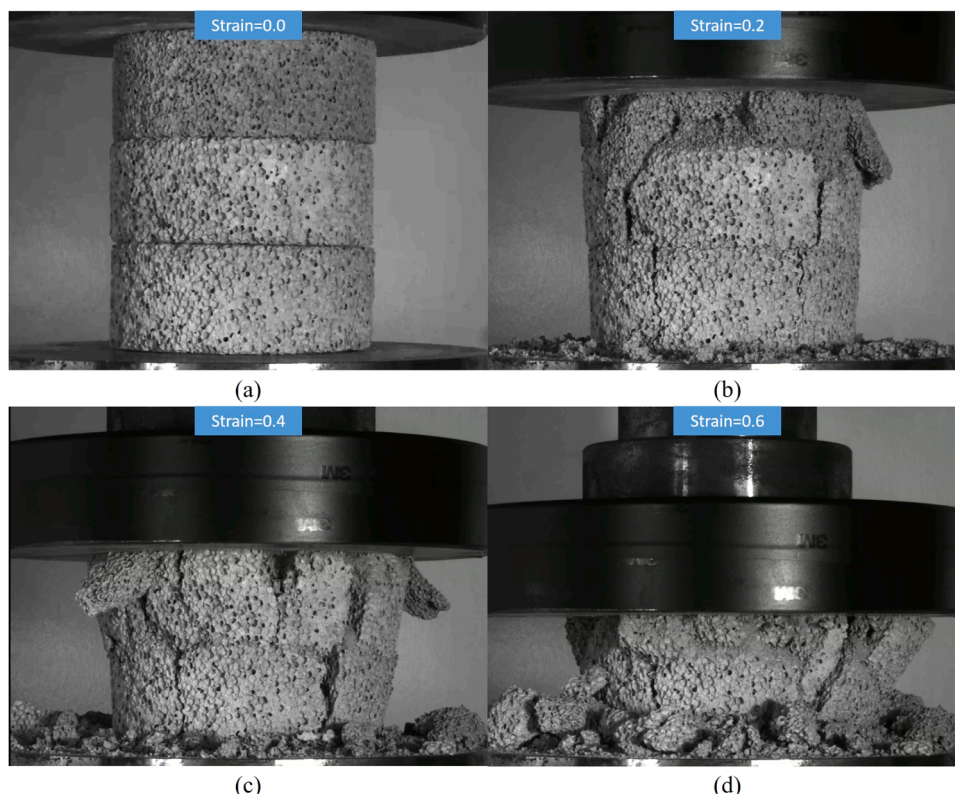


Fig. 7. Deformation process of UFC-MMM: (a) strain = 0.0, (b) strain = 0.2, (c) strain = 0.4, and (d) strain = 0.6.

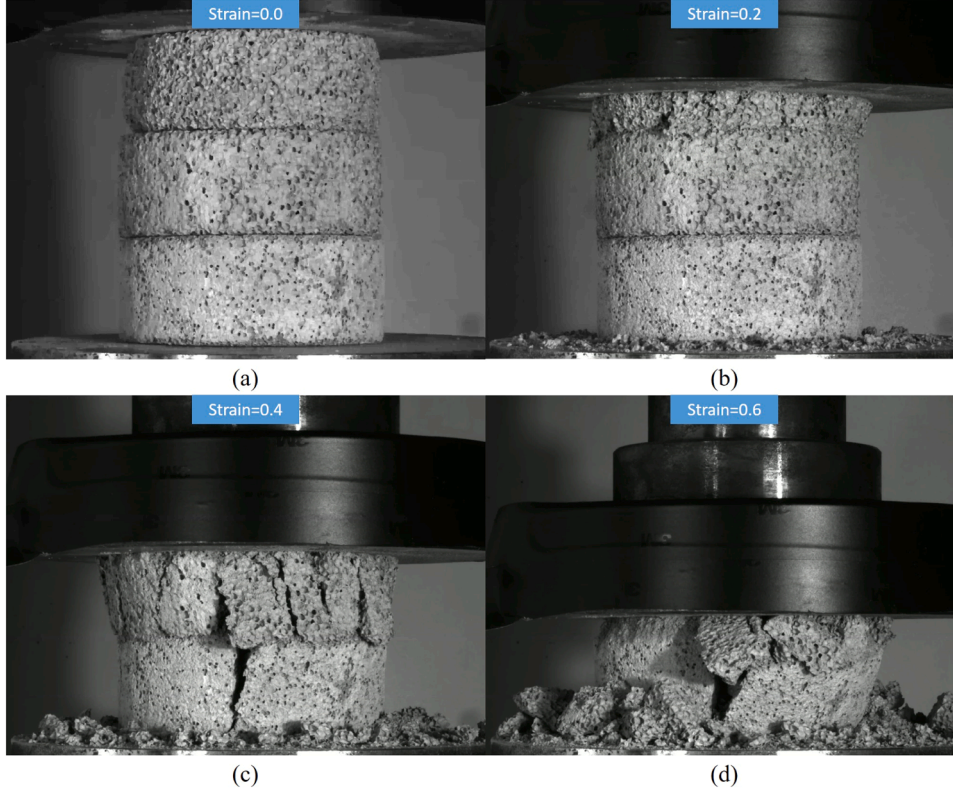


Fig. 8. Deformation process of GFC-LMH: (a) strain = 0.0, (b) strain = 0.2, (c) strain = 0.4, and (d) strain = 0.6.

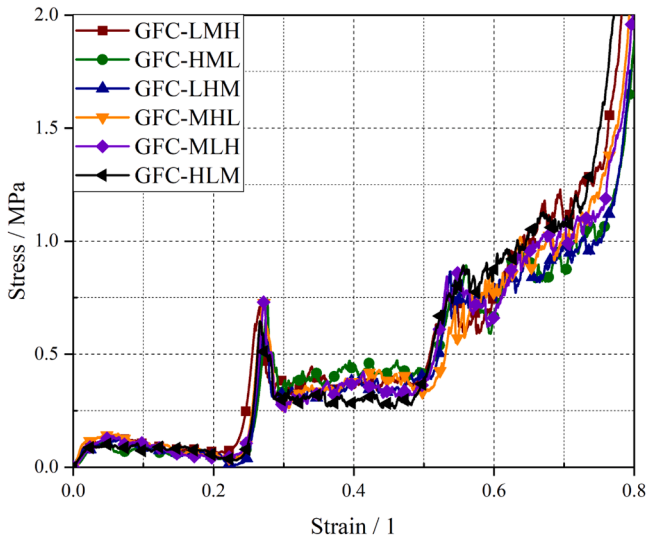


Fig. 9. Comparison of Stress-strain curves of GFC with varying gradient configurations.

consistent with the experimental specimens. It is considered that different spheres may spatially overlap, thereby forming open cells. Consequently, the porosity is computed from the actual pore volume of the final foam model. Fig. 11c depicts the presentation of the finite element model for UFC-H. To simulate the quasi-static experiments, the FC specimen is positioned amidst two inflexible plates, with the upper plate descending at a consistent velocity of 1 m/s while the lower plate remains stationary. Despite the simulation's faster loading velocity compared to the experiment, it has been proven that the specimen's two ends can attain stress equilibrium during a 1 m/s impact. Recording the

reaction force of the support plate determines the stress of the specimen. To replicate the interaction among the concrete elements, a general contact is established within the specimen with a friction coefficient of 0.4. Due to the intricate geometric shape of the pores within the specimen, regular meshing is not practical. Hence, the C4D10M tetrahedral element, which is a modified quadratic tetrahedron with 10-node and quadratic geometric order, is employed to discretize the specimen due to its remarkable suitability for intricate geometric boundaries. To ensure a precise calculation, the model is designed with a mesh size of 0.1 mm. UFC-H and UFC-L have 1,293,531 and 500,944 elements, respectively.

Defining the foam's matrix material becomes necessary once the numerical foam model is constructed. Otherwise, this model cannot be regarded as foamed concrete. To accomplish this, the matrix material of FC was described using the Johnson-Holmquist-2 (JH-2) damage model [58–60], which is widely accepted and referenced. The JH-2 model effectively describes the complete process of damage accumulation, property deterioration until crushing of brittle materials such as concrete. Hence, it finds extensive application in finite element analysis computations of brittle materials like concrete. The main framework of the JH-2 model is provided here. For convenience, more information about the model can be found at [58–60]. The strength of the JH-2 model decreases as damage accumulates. The strength is denoted in terms of the equivalent stress:

$$\sigma^* = \sigma_i^* - D(\sigma_i^* - \sigma_f^*) \quad (1)$$

where σ_i^* and σ_f^* are the normalized intact equivalent stress and the normalized fractured equivalent stress, respectively. The damage variable is represented by D . The damage values $D = 0$ and $D = 1$ represent the undamaged and completely damaged materials, respectively.

For the undamaged materials $D = 0$, the normalized equivalent stress can be expressed as:

$$\sigma_i^* = A(P^* + T^*)^N (1 + C \ln \dot{\epsilon} / \dot{\epsilon}_0) \quad (2)$$

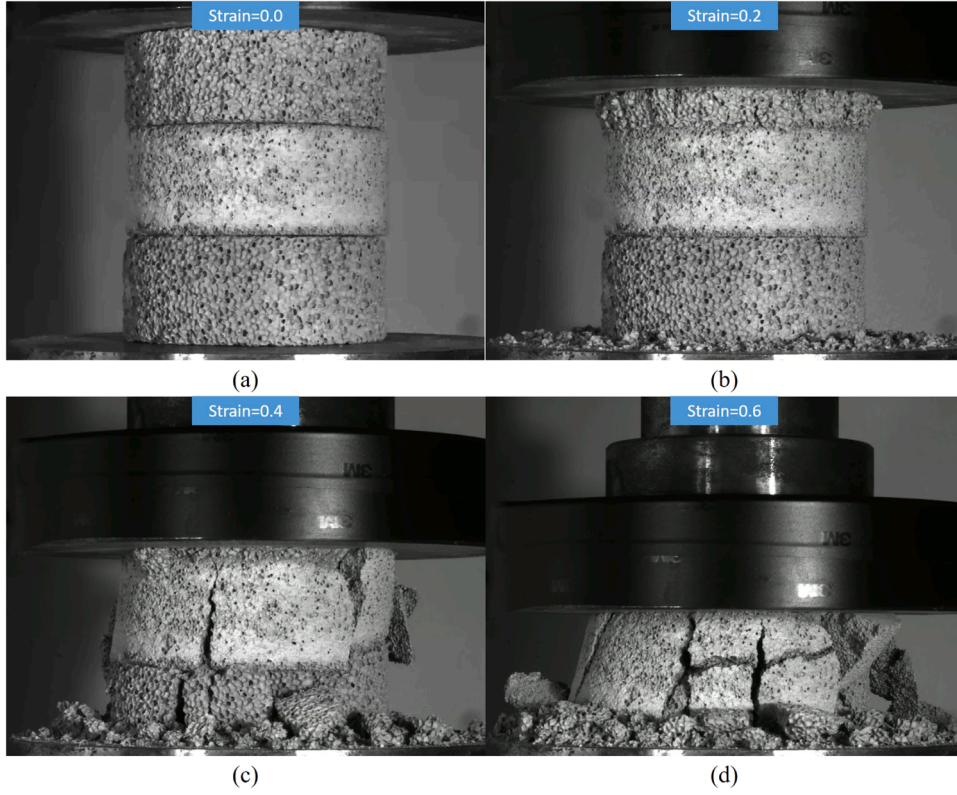


Fig. 10. Deformation process of GFC-LHM: (a) strain = 0.0, (b) strain = 0.2, (c) strain = 0.4, and (d) strain = 0.6.

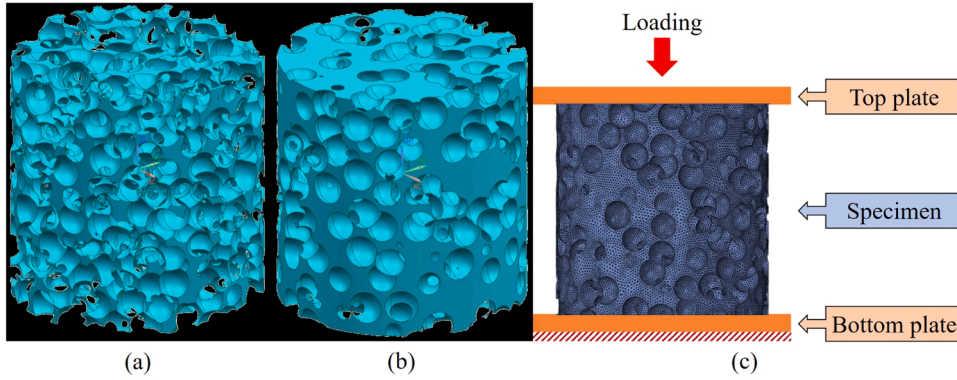


Fig. 11. Geometric models for finite element simulation: (a) UFC-L, (b) UFC-H. (c) setup of finite element simulation of UFC-H. (The loading direction is shown with a red arrow in the figure.).

For the completely damaged materials $D = 1$, the normalized equivalent stress can be expressed as:

$$\sigma_i^* = B(P^*)^M (1 + C \ln \dot{\epsilon} / \dot{\epsilon}_0) \quad (3)$$

Here, A , B , C , M and N are the material parameters. The normalized hydrostatic pressure P^* is defined as P/P_{HEL} , where P is the actual hydrostatic pressure and P_{HEL} is the hydrostatic pressure at the Hugoniot elastic limit. The normalized maximum tensile hydrostatic pressure T^* is defined as T/P_{HEL} , where T is the maximum tensile pressure that material can withstand.

The JH-2 model utilizes a damage accumulation where the damage is assumed to increase along with the plastic strain according to the following equations:

$$D = \sum \frac{\Delta \bar{\epsilon}^{pl}}{\bar{\epsilon}_f^{pl}} \quad (4)$$

where $\Delta \bar{\epsilon}^{pl}$ is the increment of the equivalent plastic strain and $\bar{\epsilon}_f^{pl}$ is the equivalent plastic strain at failure. Moreover,

$$\bar{\epsilon}_f^{pl} = D_1 (P^* + T^*)^{D_2}; \bar{\epsilon}_{fmin}^{pl} \leq \bar{\epsilon}^{pl} \leq \bar{\epsilon}_{fmax}^{pl} \quad (5)$$

where D_1 and D_2 are both the material constants. $\bar{\epsilon}_{fmin}^{pl}$ and $\bar{\epsilon}_{fmax}^{pl}$ are the minimum and maximum values of the fracture strain, respectively. The pressure-volume relationship of a brittle material in the JH-2 model is given:

$$P = \begin{cases} K_1 \mu + K_2 \mu^2 + K_3 \mu^3 & \text{if } \mu \geq 0 \\ K_1 \mu & \text{if } \mu < 0 \end{cases} \quad (6)$$

where K_1 , K_2 and K_3 are material constants. $\mu = \frac{\rho}{\rho_0} - 1$, where ρ and ρ_0 are the current and referent densities, respectively. When the material experiences failure, an additional pressure increment ΔP is included,

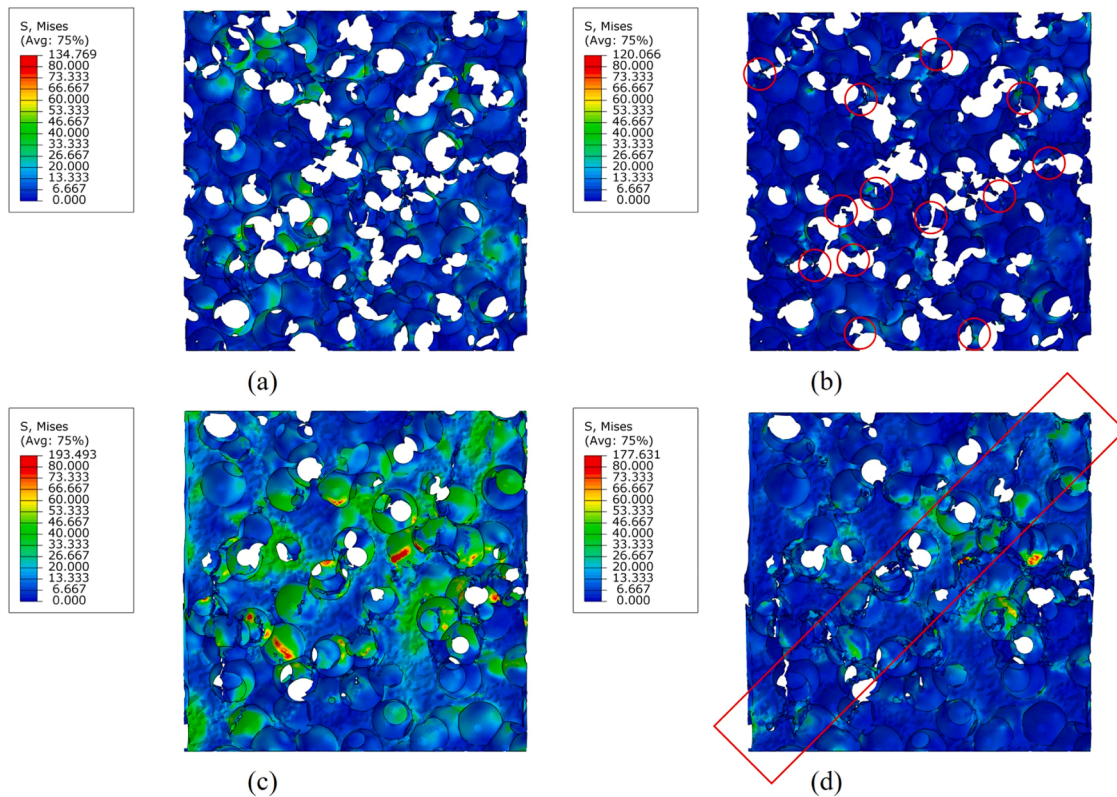


Fig. 12. Numerical deformation process of UFC-L: (a) strain = 0.005 and (b) strain = 0.01; numerical deformation process of UFC-H: (c) strain = 0.005 and (d) strain = 0.01. (The center fifth of the cross section parallel to the direction of loading is chosen for display. The red circle box indicates the location of pore-wall fracture, and the red box represents the location of crack cleavage).

which takes

$$P = K_1\mu + K_2\mu^2 + K_3\mu^3 + \Delta P \tag{7}$$

where ΔP is determined by the considered energy. As the material experiences damage, the deviatoric elastic energy ΔU decreases as the strength decreases. The decrease in elastic energy is converted into the potential energy through an increase in ΔP , which is:

$$\Delta P_{t+\Delta t} = -K_1\mu_{t+\Delta t} + \sqrt{(K_1\mu_{t+\Delta t} + \Delta P_t)^2 + 2\beta K_1 \Delta U} \tag{8}$$

where β is the fraction of the elastic energy increase converted into potential energy ($0 \leq \beta \leq 1$).

Given the complexity of concrete materials, obtaining all necessary model parameters through simple experiments can be challenging. The main goal of the finite element simulations is to determine the distribution of stress within the specimen and clarify the differences in failure modes of FC with varying porosities. Therefore, this study does not strive for the simulation model to match the stress values of the experimental curves. Instead, it necessitates that the simulation model accurately reflects the deformation characteristics of the concrete matrix. Hence, the material parameters utilized in this study are derived from references that have been verified through experiments. These material

parameters, which have been confirmed by experimental data in references [59,60], can be found in Table 1. To model the matrix material of foamed concrete, these parameters were integrated into Abaqus/Explicit as a user-defined material subroutine. To circumvent potential unreliability, the parameters of the matrix material have been left unaltered. The study employs the space holder technique to model the foam, while the JH-2 model is used to characterize its concrete matrix, resulting in a highly effective simulation approach for foamed concrete. Further research could potentially broaden its scope to include other areas of study, such as investigating the effect of strain rate on matrix materials and exploring the effects of strain hardening, among various other possibilities.

Finite element modeling is employed to enhance comprehension due to the difficulties in experimentally acquiring stress distribution within the specimen. Fig. 12 presents the stress contour of UFC-L and UFC-H at strains of 0.005 and 0.01, respectively. The distribution of stress within one-fifth of the cross-sectional diameter is illustrated in Fig. 12. This reveals that the UFC-L exhibits stress concentration at the pore-wall junction (as indicated by the red and green regions in Fig. 12a), where pore-wall failure transpires under subsequent loading (Fig. 12b). The UFC-L possesses a substantial number of pores, as denoted by the red circle in Fig. 12b, resulting in a higher number of weaker pore walls. The powdering failure mode occurs as a result of the widespread distribution

Table 1
Matrix concrete's material parameters for the JH-2 model [58–60].

ρ (kg/m ³)	G (GPa)	A	B	N	C	
2440	14.86	0.79	1.6	0	0.007	
M	ϵ_0	S_{max}	T (GPa)	$\bar{\epsilon}_{fmin}^{pl}$	$\bar{\epsilon}_{fmax}^{pl}$	P_{HEL} (MPa)
0.61	1	7	0.00354	0.001	1	48
D_1	D_2	K_1 (GPa)	K_2 (GPa)	K_3 (GPa)	HEL (MPa)	
0.04	1	85	-171	208	80	

of these delicate pore walls within the specimen during compression. Conversely, UFC-H has fewer pores and thicker pore walls (Fig. 12c), which precludes the powdering failure mode by ensuring adequate pore-wall strength. However, the existence of a dominant crack within the specimen, as depicted in Fig. 12d, results in the splitting failure mode. The aforementioned differences in failure modes epitomize the most characteristic features of specimens with varying porosities. As the loading strain escalates, UFC-L continues to experience pore-wall failure, whereas UFC-H fails along the dominant crack. Hence, the findings of this research provide additional insights and a deeper understanding of the observed experimental phenomena. In summary, varying porosities influence the cell-wall strength of foam concrete, which subsequently leads to differential failure modes.

4. Phenomenological model

The existing body of literature on FC primarily employs statistical models [36–41] based on material properties, such as the relationship between compressive strength and density. Nevertheless, there is a noticeable lack of models that can forecast the entire Stress–strain curve of FC. According to Wang et al. [61], a statistical model was proposed to take into account the deformation mechanism of the mesostructure and thus capture all features of Stress–strain curves exhibited by foams. This six-parameter statistical model is articulated in Eq. (9)

$$\sigma(\varepsilon) = (E\varepsilon - B)e^{-(\varepsilon/\lambda)^k} + B + \frac{C\varepsilon}{(\varepsilon_m - \varepsilon)^2} \quad (9)$$

The elastic modulus, collapse stress, and strain hardening parameter of the foam specimen are denoted as E , B , C , respectively. The scale parameter and the shape parameter are λ and k , respectively. ε_m is the maximal strain of the foam specimen and usually identified as 1. The scale parameter and the shape parameter are both insensitive to the relative density and are determined as 0.0335 and 1.469, respectively [62]. Eq. (9) was fitted to the experimental data of UFC specimens using the LAR–Levenberg–Marquardt method. Eq. (10) expresses the relationship between the relative density and the elastic modulus, plateau stress, and hardening parameter in an exponential law:

$$\begin{cases} E(\bar{\rho}) = 461.4\bar{\rho}^{2.009} \\ B(\bar{\rho}) = 12.77\bar{\rho}^{2.872} \\ C(\bar{\rho}) = 1.068\bar{\rho}^{3.408} \end{cases} \quad (10)$$

Thus, Eq. (9) can be rewritten as

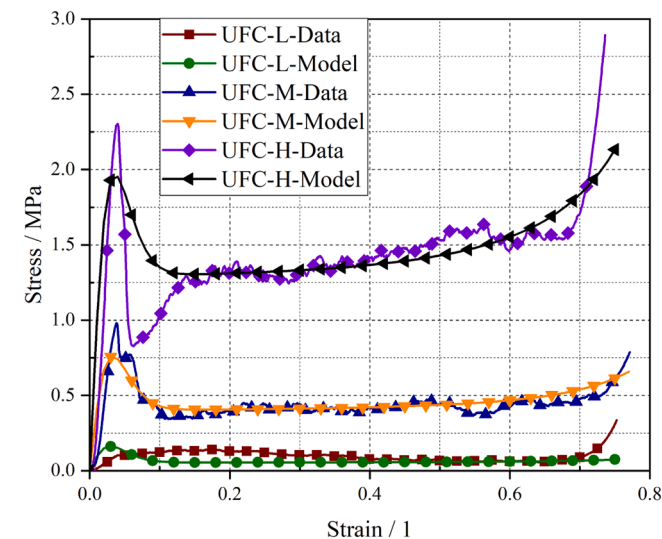


Fig. 13. Stress–strain curves for various specimens (UFC-L, UFC-M, and UFC-H) and comparing them with statistical model and experimental data.

$$\sigma(\varepsilon) = (461.4\bar{\rho}^{2.009}\varepsilon - 12.77\bar{\rho}^{2.872})e^{-(\varepsilon/0.0335)^{1.469}} + 12.77\bar{\rho}^{2.872} + \frac{1.068\bar{\rho}^{3.408}\varepsilon}{(1 - \varepsilon)^2} \quad (11)$$

Fig. 13 displays the Stress–strain curves for various specimens (UFC-L, UFC-M, and UFC-H), comparing the experimental data with the statistical model. The agreement between the prediction results of the model and the experimental data is evident.

The Stress–strain curve of GFC is an amalgamation of the strengths of various layers of UFCs, implying that the mechanical response of the GFC can be predicted by integrating the Stress–strain curves of different UFCs. For example, by shifting the Stress–strain curves from the model in Fig. 13 along the x-axis with a strain increment of 0, 0.25, and 0.5 for UFC-L, UFC-M, and UFC-H, respectively, the Stress–strain curves of GFC-LMH can be juxtaposed with the experimental data and statistical model. In the experiments, the densified strain of GFCs is around 0.75, which refers to the point where the stress rapidly increases from the plateau stage to the densification stage. Considering that the GFC in this study comprises three layers, the designated increase in strain was decided to be 0.25. As depicted in Fig. 14, accurate prediction results are obtained for both UFC-L and UFC-M, while the predicted value for UFC-H exceeds the experimental results. The reason for this difference is due to the failure of the second layer, leading to uneven contact surfaces and simultaneous cracking of the third layer. Consequently, the final deforming layer in the brittle gradient foam cannot attain the strength of the corresponding uniform foam. In previous researches [47,48,52,54], plastic gradient foam showed a different behavior compared to the phenomenon described here. The Stress–strain curve of the foam in prior studies continuously increased. The initial deforming layer did not have a significant effect on the subsequent deforming layer.

5. Conclusions

The focus of this research is to investigate how density affects the deformation mechanism of foamed concrete, including both UFC and GFC. The findings underscore that UFC with a higher density exhibits greater compressive strength compared to its low-density counterpart. Moreover, the failure modes for these two types of concrete are distinct. Low-density UFC is characterized by weak pore walls that fracture under compressive loading, culminating in a powdering failure mode. On the other hand, UFC with high density exhibits excellent capacity to bear loads, resulting in fewer fractures of pore walls during loading. This

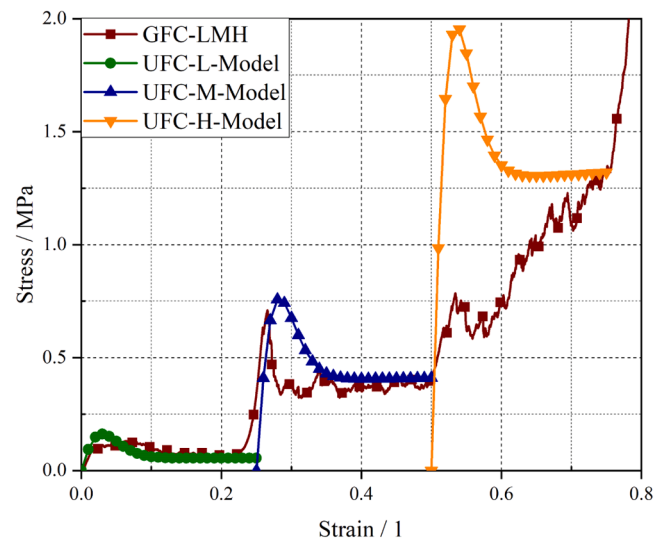


Fig. 14. Stress–strain curves of specimen GFC-LMH by comparing the experimental data with a statistical model.

ultimately leads to large penetrating cracks and a splitting failure mode. In the case of GFC, which comprises three layers of UFCs with varying densities, each layer deforms in a sequence from low to high density. Each layer manifests a failure mode that corresponds to its specific density. However, it is noteworthy that the last-deforming layer in GFC cannot achieve the strength of the corresponding UFC. Cause the uneven contact surface causes cracks to appear in the third layer when the second layer is compressed. Finally, a statistical model is developed to represent the compressive strength of foamed concrete. The predictions generated by this model closely match the experimental findings.

CRedit authorship contribution statement

Liangliang Xu: Conceptualization, Methodology, Validation, Formal analysis, Investigation, Writing – original draft, Writing – review & editing, Visualization. **Xi Li:** Investigation, Writing – review & editing, Visualization. **Muhammad Atif:** Writing – review & editing. **Yulong Li:** Conceptualization, Resources, Writing – review & editing, Supervision, Funding acquisition.

Declaration of Competing Interest

The authors declare that they have no known competing financial interests or personal relationships that could have appeared to influence the work reported in this paper.

Data availability

Data will be made available on request.

Acknowledgments

This work is financially supported by the National Natural Science Foundation of China [grant number 11527803] and the Higher Education Discipline Innovation Project [grant number BP0719007].

Supplementary materials

Supplementary material associated with this article can be found, in the online version, at [doi:10.1016/j.tws.2023.111487](https://doi.org/10.1016/j.tws.2023.111487).

References

- [1] Y.H.M. Amran, N. Farzadnia, A.A. Abang Ali, Properties and applications of foamed concrete; a review, *Constr. Build. Mater.* 101 (2015) 990–1005, <https://doi.org/10.1016/j.conbuildmat.2015.10.112>.
- [2] M.A. Othuman Mydin, Y.C. Wang, Structural performance of lightweight steel-foamed concrete–steel composite walling system under compression, *Thin-Walled Struct.* 49 (2011) 66–76, <https://doi.org/10.1016/j.tws.2010.08.007>.
- [3] H. Zhou, K. Jia, X. Wang, M.-X. Xiong, Y. Wang, Experimental and numerical investigation of low velocity impact response of foam concrete filled auxetic honeycombs, *Thin-Walled Struct.* 154 (2020), 106898, <https://doi.org/10.1016/j.tws.2020.106898>.
- [4] C. Yuan, Z. Wenhua, Z. Lei, Z. Wanting, Z. Yunsheng, Dynamic impact compressive performance of expanded polystyrene (EPS)-foamed concrete, *Arch. Civ. Mech. Eng.* 22 (2022) 164, <https://doi.org/10.1007/s43452-022-00486-6>.
- [5] V.S. Deshpande, N.A. Fleck, Isotropic constitutive models for metallic foams, *J. Mech. Phys. Solids.* 48 (2000) 1253–1283, [https://doi.org/10.1016/S0022-5096\(99\)00082-4](https://doi.org/10.1016/S0022-5096(99)00082-4).
- [6] S. Talebi, R. Hedayati, M. Sadighi, Dynamic crushing behavior of closed-cell aluminum foams based on different space-filling unit cells, *Arch. Civ. Mech. Eng.* 21 (2021) 99, <https://doi.org/10.1007/s43452-021-00251-1>.
- [7] B. Koohbor, N. Pagliocca, G. Youssef, A multiscale experimental approach to characterize micro-to-macro transition length scale in polymer foams, *Mech. Mater.* 161 (2021), 104006, <https://doi.org/10.1016/j.mechmat.2021.104006>.
- [8] J. Lubliner, J. Oliver, S. Oller, E. Onate, A plastic-damage model for concrete, *Int. J. Solids Struct.* 25 (1989) 299–326, [https://doi.org/10.1016/0020-7683\(89\)90050-4](https://doi.org/10.1016/0020-7683(89)90050-4).
- [9] J.F. Castillo-Lara, E.A. Flores-Johnson, A. Valadez-Gonzalez, P.J. Herrera-Franco, J.G. Carrillo, P.I. Gonzalez-Chi, E. Agaliotis, Q.M. Li, Mechanical behaviour of composite sandwich panels with foamed concrete core reinforced with natural fibre in four-point bending, *Thin-Walled Struct.* 169 (2021), 108457, <https://doi.org/10.1016/j.tws.2021.108457>.
- [10] H. Zhou, J. Fan, X. Wang, G. Ma, S. Yu, Y. Wang, Protection performance of sacrificial cladding with foam concrete filled aluminum tubes under blast loading, *Int. J. Impact Eng.* 179 (2023), 104633, <https://doi.org/10.1016/j.ijimpeng.2023.104633>.
- [11] L.J. Gibson, M.F. Ashby, *Cellular Solids: Structure and Properties*, Cambridge University Press, 1999, <https://doi.org/10.1017/cbo9781139878326>.
- [12] Y. Duan, B. Du, X. Shi, B. Hou, Y. Li, Quasi-static and dynamic compressive properties and deformation mechanisms of 3D printed polymeric cellular structures with Kelvin cells, *Int. J. Impact Eng.* 132 (2019), 103303, <https://doi.org/10.1016/j.ijimpeng.2019.05.017>.
- [13] C. Shi, Z. Wu, J. Xiao, D. Wang, Z. Huang, Z. Fang, A review on ultra high performance concrete: part I. Raw materials and mixture design, *Constr. Build. Mater.* 101 (2015) 741–751, <https://doi.org/10.1016/j.conbuildmat.2015.10.088>.
- [14] R. Zhang, X. Ma, D. Jiang, Y. Wang, L. Wu, X. Zhi, Experimental study on a novel steel-PU foam-concrete-tube multilayer energy absorbing panel under impact loading, *Thin-Walled Struct.* 189 (2023), 110880, <https://doi.org/10.1016/j.tws.2023.110880>.
- [15] X. Wang, X. Zhang, L. Song, H. Zhou, Y. Wang, H. Zhang, P. Cong, Mitigating confined blast response of buried steel box structure with foam concrete, *Thin-Walled Struct.* 169 (2021), 108473, <https://doi.org/10.1016/j.tws.2021.108473>.
- [16] Z.Q. Zhang, J.L. Yang, Q.M. Li, An analytical model of foamed concrete aircraft arresting system, *Int. J. Impact Eng.* 61 (2013) 1–12, <https://doi.org/10.1016/j.ijimpeng.2013.05.006>.
- [17] J. Xiao, H. Zhang, S. Zou, Z. Duan, Y. Ma, Developing recycled foamed concrete for engineered material arresting system, *J. Build. Eng.* 53 (2022), 104555, <https://doi.org/10.1016/j.jobe.2022.104555>.
- [18] Z. Xu, Z. Chen, S. Yang, Seismic behavior of cold-formed steel high-strength foamed concrete shear walls with straw boards, *Thin-Walled Struct.* 124 (2018) 350–365, <https://doi.org/10.1016/j.tws.2017.12.032>.
- [19] X. Shi, J. Huang, Q. Su, Experimental and numerical analyses of lightweight foamed concrete as filler for widening embankment, *Constr. Build. Mater.* 250 (2020), 118897, <https://doi.org/10.1016/j.conbuildmat.2020.118897>.
- [20] G. Wang, Z. Deng, H. Xu, D. Wang, Z. Lu, Application of foamed concrete backfill in improving antiexplosion performance of buried pipelines, *J. Mater. Civ. Eng.* 33 (2021), [https://doi.org/10.1061/\(ASCE\)MT.1943-5533.0003630](https://doi.org/10.1061/(ASCE)MT.1943-5533.0003630).
- [21] X. Tan, W. Chen, D. Yang, H. Liu, A.H.C. Chan, Experimental and theoretical studies on effect of height-to-diameter ratios on failure forms and mechanical characteristics of foamed concrete, *J. Mater. Civ. Eng.* (2019) 31, [https://doi.org/10.1061/\(ASCE\)MT.1943-5533.0002557](https://doi.org/10.1061/(ASCE)MT.1943-5533.0002557).
- [22] R. Othman, R.P. Jaya, K. Muthusamy, M. Sulaiman, Y. Duraisamy, M.M.A. B. Abdullah, A. Przybyl, W. Sochacki, T. Skrzypczak, P. Vizureanu, A.V. Sandu, Relation between density and compressive strength of foamed concrete, *Materials (Basel)* 14 (2021) 2967, <https://doi.org/10.3390/ma14112967>.
- [23] A. Just, B. Middendorf, Microstructure of high-strength foam concrete, *Mater. Charact.* 60 (2009) 741–748, <https://doi.org/10.1016/j.matchar.2008.12.011>.
- [24] T.T. Nguyen, H.H. Bui, T.D. Ngo, G.D. Nguyen, Experimental and numerical investigation of influence of air-voids on the compressive behaviour of foamed concrete, *Mater. Des.* 130 (2017) 103–119, <https://doi.org/10.1016/j.matdes.2017.05.054>.
- [25] L. Hou, J. Li, Z. Lu, Y. Niu, Influence of foaming agent on cement and foam concrete, *Constr. Build. Mater.* 280 (2021), 122399, <https://doi.org/10.1016/j.conbuildmat.2021.122399>.
- [26] E. Eltayeb, X. Ma, Y. Zhuge, O. Youssf, J.E. Mills, Influence of rubber particles on the properties of foam concrete, *J. Build. Eng.* 30 (2020), 101217, <https://doi.org/10.1016/j.jobe.2020.101217>.
- [27] M. Abd Elrahman, P. Sikora, S.-Y. Chung, D. Stephan, The performance of ultra-lightweight foamed concrete incorporating nanosilica, *Arch. Civ. Mech. Eng.* 21 (2021) 79, <https://doi.org/10.1007/s43452-021-00234-2>.
- [28] S. Zhang, X. Qi, S. Guo, L. Zhang, J. Ren, A systematic research on foamed concrete: the effects of foam content, fly ash, slag, silica fume and water-to-binder ratio, *Constr. Build. Mater.* 339 (2022), 127683, <https://doi.org/10.1016/j.conbuildmat.2022.127683>.
- [29] O. Gencel, B. Balci, O.Y. Bayraktar, M. Nodehi, A. Sari, G. Kaplan, G. Hekimoglu, A. Gholampour, A. Benli, T. Ozbakkaloglu, The effect of limestone and bottom ash sand with recycled fine aggregate in foam concrete, *J. Build. Eng.* 54 (2022), 104689, <https://doi.org/10.1016/j.jobe.2022.104689>.
- [30] X. Chen, D. Shi, J. Zhang, X. Cheng, Experimental investigation of the residual physical and mechanical properties of foamed concrete exposed to high temperatures, *J. Mater. Civ. Eng.* 33 (2021), [https://doi.org/10.1061/\(ASCE\)MT.1943-5533.0003779](https://doi.org/10.1061/(ASCE)MT.1943-5533.0003779).
- [31] H. Xi, Y. Yao, Y. Sun, B. Mobasher, Y. Liu, H. Ma, Compressive and thermal properties of foamed concrete at high temperature, *J. Sustain. Cem. Mater.* (2021) 1–25, <https://doi.org/10.1080/21650373.2021.1961639>.
- [32] B. Wang, Y. Chen, H. Fan, F. Jin, Investigation of low-velocity impact behaviors of foamed concrete material, *Compos. Part B Eng.* 162 (2019) 491–499, <https://doi.org/10.1016/j.compositesb.2019.01.021>.
- [33] S. Feng, Y. Zhou, Y. Wang, M. Lei, Experimental research on the dynamic mechanical properties and damage characteristics of lightweight foamed concrete under impact loading, *Int. J. Impact Eng.* 140 (2020), 103558, <https://doi.org/10.1016/j.ijimpeng.2020.103558>.
- [34] X. Tan, W. Chen, H. Liu, A.H.C. Chan, Stress-strain characteristics of foamed concrete subjected to large deformation under uniaxial and triaxial compressive loading, *J. Mater. Civ. Eng.* 30 (2018), [https://doi.org/10.1061/\(ASCE\)MT.1943-5533.0002311](https://doi.org/10.1061/(ASCE)MT.1943-5533.0002311).

- [35] H. Zhang, M. Liu, Z. Shuo, Z. Zhao, Y. Sun, X. Song, H. Wang, X. Zhang, J. Wu, An experimental investigation of the triaxial shear behaviors of silt-based foamed concrete, *Case Stud. Constr. Mater.* 15 (2021) e00713, <https://doi.org/10.1016/j.cscm.2021.e00713>.
- [36] E.P. Kearsley, P.J. Wainwright, Porosity and permeability of foamed concrete, *Cem. Concr. Res.* 31 (2001) 805–812, [https://doi.org/10.1016/S0008-8846\(01\)00490-2](https://doi.org/10.1016/S0008-8846(01)00490-2).
- [37] E... Kearsley, P... Wainwright, The effect of porosity on the strength of foamed concrete, *Cem. Concr. Res.* 32 (2002) 233–239, [https://doi.org/10.1016/S0008-8846\(01\)00665-2](https://doi.org/10.1016/S0008-8846(01)00665-2).
- [38] W. Zhao, J. Huang, Q. Su, T. Liu, Models for strength prediction of high-porosity cast-in-situ foamed concrete, *Adv. Mater. Sci. Eng.* 18 (2018) 1–10, <https://doi.org/10.1155/2018/3897348>.
- [39] F. Rao, Z. Zhang, G. Ye, J. Liu, Micromechanical modeling on compressive behavior of foamed concrete, *J. Mater. Civ. Eng.* 33 (2021), [https://doi.org/10.1061/\(ASCE\)MT.1943-5533.0003935](https://doi.org/10.1061/(ASCE)MT.1943-5533.0003935).
- [40] E.K.K. Nambiar, K. Ramamurthy, Models for strength prediction of foam concrete, *Mater. Struct.* 41 (2008) 247–254, <https://doi.org/10.1617/s11527-007-9234-0>.
- [41] H. Guo, W. Guo, Y. Shi, Computational modeling of the mechanical response of lightweight foamed concrete over a wide range of temperatures and strain rates, *Constr. Build. Mater.* 96 (2015) 622–631, <https://doi.org/10.1016/j.conbuildmat.2015.08.064>.
- [42] T. Nguyen, A. Ghazlan, A. Kashani, S. Bordas, T. Ngo, 3D meso-scale modelling of foamed concrete based on X-ray computed tomography, *Constr. Build. Mater.* 188 (2018) 583–598, <https://doi.org/10.1016/j.conbuildmat.2018.08.085>.
- [43] J.-S. Kim, S.-Y. Chung, T.-S. Han, D. Stephan, M.A. Elrahman, Correlation between microstructural characteristics from micro-CT of foamed concrete and mechanical behaviors evaluated by experiments and simulations, *Cem. Concr. Compos.* 112 (2020), 103657, <https://doi.org/10.1016/j.cemconcomp.2020.103657>.
- [44] J. Yuan, W. Chen, X. Tan, W. Yang, D. Yang, H. Yu, B. Zhou, B. Yang, Study on the permeability characteristics of foamed concrete using a pore-scale model from X-ray microcomputed tomography image reconstruction and numerical simulation, *J. Mater. Civ. Eng.* (2021) 33, [https://doi.org/10.1061/\(ASCE\)MT.1943-5533.0003735](https://doi.org/10.1061/(ASCE)MT.1943-5533.0003735).
- [45] L. Jin, S. Chen, Y. Zhao, Q. Zeng, Z. Huang, M. Li, Y. Shi, Characterizing the foam-shell microstructure of industrial ultra-light foamed concrete cast under different temperatures, *Mater. Charact.* 173 (2021), 110938, <https://doi.org/10.1016/j.matchar.2021.110938>.
- [46] X. Wang, L. Liu, H. Zhou, T. Song, Q. Qiao, H. Zhang, Improving the compressive performance of foam concrete with ceramsite: experimental and meso-scale numerical investigation, *Mater. Des.* 208 (2021), 109938, <https://doi.org/10.1016/j.matdes.2021.109938>.
- [47] A.H. Brothers, D.C. Dunand, Mechanical properties of a density-graded replicated aluminum foam, *Mater. Sci. Eng. A.* 489 (2008) 439–443, <https://doi.org/10.1016/j.msea.2007.11.076>.
- [48] Y. Duan, Y. Ding, Z. Liu, N. Hou, X. Zhao, H. Liu, Z. Zhao, B. Hou, Y. Li, Effects of cell size vs. cell-wall thickness gradients on compressive behavior of additively manufactured foams, *Compos. Sci. Technol.* 199 (2020), 108339, <https://doi.org/10.1016/j.compscitech.2020.108339>.
- [49] B. Koohbor, S. Ravindran, A. Kidane, In situ deformation characterization of density-graded foams in quasi-static and impact loading conditions, *Int. J. Impact Eng.* 150 (2021), 103820, <https://doi.org/10.1016/j.ijimpeng.2021.103820>.
- [50] H. Zhang, B. Chang, K. Peng, J. Yu, Z. Zheng, Anti-blast analysis and design of a sacrificial cladding with graded foam-filled tubes, *Thin-Walled Struct.* 182 (2023), 110313, <https://doi.org/10.1016/j.tws.2022.110313>.
- [51] O. Rahman, K.Z. Uddin, J. Muthulingam, G. Youssef, C. Shen, B. Koohbor, Density-graded cellular solids: mechanics, fabrication, and applications, *Adv. Eng. Mater.* 24 (2022), <https://doi.org/10.1002/adem.202100646>.
- [52] Y. Duan, X. Zhao, Z. Liu, N. Hou, H. Liu, B. Du, B. Hou, Y. Li, Dynamic response of additively manufactured graded foams, *Compos. Part B Eng.* 183 (2020), 107630, <https://doi.org/10.1016/j.compositesb.2019.107630>.
- [53] H. Zhou, X. Zhang, X. Wang, H. Zhang, T. Song, Improving energy absorption capacity of foam concrete with gradient and layered architecture, *Constr. Build. Mater.* 319 (2022), 126140, <https://doi.org/10.1016/j.conbuildmat.2021.126140>.
- [54] N. Gupta, A functionally graded syntactic foam material for high energy absorption under compression, *Mater. Lett.* 61 (2007) 979–982, <https://doi.org/10.1016/j.matlet.2006.06.033>.
- [55] L. Ying, S. Wang, T. Gao, M. Dai, P. Hu, Y. Wang, Crashworthiness analysis and optimization of multi-functional gradient foam-aluminum filled hierarchical thin-walled structures, *Thin-Walled Struct.* 189 (2023), 110906, <https://doi.org/10.1016/j.tws.2023.110906>.
- [56] M. Smeets, P. Kouvaka, K. Uddin, B. Koohbor, G. Youssef, Full-field analyses of density-graded elastomeric foams under quasistatic and impact loadings, *Adv. Eng. Mater.* (2023), <https://doi.org/10.1002/adem.202300994>.
- [57] L. Xu, Y. Duan, Y. Li, Porosity, gradient and impact velocity effects on compressive response of foamed concrete, *Constr. Build. Mater.* 315 (2022), 125616, <https://doi.org/10.1016/j.conbuildmat.2021.125616>.
- [58] H. Xu, H.M. Wen, A computational constitutive model for concrete subjected to dynamic loadings, *Int. J. Impact Eng.* 91 (2016) 116–125, <https://doi.org/10.1016/j.ijimpeng.2016.01.003>.
- [59] C. Oucif, L.M. Mauludin, Numerical modeling of high velocity impact applied to reinforced concrete panel, *Undergr. Space* 4 (2019) 1–9, <https://doi.org/10.1016/j.undsp.2018.04.007>.
- [60] C. Oucif, J.S. Kalyana Rama, K. Shankar Ram, F. Abed, Damage modeling of ballistic penetration and impact behavior of concrete panel under low and high velocities, *Def. Technol.* 17 (2021) 202–211, <https://doi.org/10.1016/j.dt.2020.03.013>.
- [61] S. Wang, Z. Zheng, C. Zhu, Y. Ding, J. Yu, Crushing and densification of rapid prototyping polylactide foam: meso-structural effect and a statistical constitutive model, *Mech. Mater.* 127 (2018) 65–76, <https://doi.org/10.1016/j.mechmat.2018.09.003>.
- [62] Y. Duan, X. Chen, B. Yin, X. Zhao, Z. Zhao, B. Hou, Y. Li, Understanding the effect of defects on compressive behaviors of closed-cell foams: experiment and statistical model, *Compos. Part B Eng.* 244 (2022), 110179, <https://doi.org/10.1016/j.compositesb.2022.110179>.